Physica Scripta

RECEIVED
31 March 2025

REVISED
4 July 2025

ACCEPTED FOR PUBLICATION
16 July 2025

PUBLISHED
28 July 2025

PAPER

Calculating and predicting of transverse momentum and entropy based on rapidity in Au-Au nuclear collisions by HRG, Tsallis and ANFIS models at NICA energies

Mahmoud Nasar[1,2,*], **E H Aamer**[3] and **Mohammed Aish**[2,4]

[1] Physics Department, Faculty of Science, Benha University, 13518, Benha, Egypt
[2] Egypt Academy of Scientific Research and Technology (ASRT), 101 Kasr Al Aini Street, 11516, Cairo, Egypt
[3] Ain Shams University, Faculty of Education, Physics Department, 11771, Roxy, Cairo, Egypt
[4] Physics Department, Faculty of Science, Menoufia University, 32928, Menofia, Egypt
[*] Author to whom any correspondence should be addressed.

E-mail: mahmoud.nasar@fsc.bu.edu.eg

Keywords: particle spectra, ANFIS, NICA energies

Abstract

In this work, we calculate and predict the transverse momentum spectra (p_T) and entropy per unit rapidity ($d\Omega/dy$) for hadrons ($\pi^{\pm}$, $K^{\pm}$, p, and $\bar{p}$) produced in central Au–Au collisions at $\sqrt{s_{\rm NN}} = 7.7$ and 11.5 GeV, corresponding to the energies accessible at NICA (Nuclotron-based Ion Collider fAcility). The particle momentum distribution are analyzed using both the Hadron Resonance Gas (HRG) model and the Tsallis distribution, each applied in their suitable momentum regions. Furthermore, a data-driven Adaptive Neuro-Fuzzy Inference System (ANFIS) model is employed to replicate and extrapolate the spectra based on measured data. The ANFIS predictions show strong consistency with experimental results and serve as an alternative approach for estimating physical observables in regions where direct data is limited. The entropy per rapidity is then calculated using the fitted spectra and source radii from femtoscopic measurements. We observe that the combined Tsallis-HRG description and ANFIS model yield comparable results within uncertainties, supporting the viability of ANFIS for modeling particle production at intermediate energies.

1. Introduction

Relativistic nucleus–nucleus collisions in the beam energy range of 4–11 GeV have drawn increasing attention due to their potential to produce high strangeness content [1] and large baryon densities [2–4] at moderate temperatures. These conditions make this regime particularly suitable for exploring the properties of dense nuclear matter and investigating the QCD (Quantum Chromodynamics) phase structure.

Recent experimental efforts, including low-energy scans at the SPS [5] and upcoming heavy-ion programs at the NICA facility at JINR, Dubna [6], have revitalized interest in this intermediate region of the QCD phase diagram. Unlike the well-characterized extremes-cold, dense matter and hot, baryon-sparse matter-this domain remains relatively unexplored, both theoretically and experimentally. Of particular interest is the possibility that the QCD critical point, marking the onset of a first-order phase transition between hadronic matter and a deconfined quark–gluon plasma (QGP), may lie within reach of collisions at these energies [7, 8].

Lattice QCD calculations suggest that the transition from the hadronic phase to the QGP is a smooth crossover at low baryon chemical potential (μ_B) [9]. High-energy experiments such as those at the LHC (Large Hadron Collider) and RHIC (Relativistic Heavy Ion Collider) have focused on studying this crossover region under near-zero μ_B conditions [10, 11]. However, future experiments at NICA and FAIR (Facility for Antiproton and Ion Research), as well as ongoing efforts at RHIC (e.g., the STAR experiment), are targeting the high-μ_B regime to explore the QCD matter under different initial conditions [12].

Transverse momentum (p_T) spectra serve as a crucial probe of the thermodynamic and dynamical evolution of the produced system in heavy-ion collisions [13]. These spectra reflect thermalization, collective flow, and particle production mechanisms and are often modeled using relativistic hydrodynamics [14, 15]. Entropy per unit rapidity ($d\Omega/dy$), which is approximately conserved from early thermalization through to kinetic freeze-out, offers a complementary observable that encodes information about the degrees of freedom and thermal state of the medium [10, 16, 17].

In this work, we predict the p_T spectra of identified particles ($\pi^{\pm}$, $K^{\pm}$, p, and $\bar{p}$) produced in central Au–Au collisions at $\sqrt{s_{NN}} = 7.7$ and 11.5 GeV using the Adaptive Neuro-Fuzzy Inference System (ANFIS) model [18–20]. ANFIS belongs to a broader class of AI-based soft computing techniques that have become increasingly valuable in modeling non-linear systems in high-energy physics [21–25]. The complexity of heavy-ion collisions, where the relationships between initial conditions and final-state observables are highly non-linear, makes AI a compelling alternative to traditional analytical models [26].

Various AI techniques-including Artificial Neural Networks (ANN), Genetic algorithms (GA), Gene Expression Programming (GEP), and ANFIS-have shown strong potential in reproducing and predicting experimental results [21, 25]. ANNs are particularly appealing due to their learning capabilities and their ability to extract complex features from data [27]. ANFIS, which integrates neural networks with fuzzy logic, has demonstrated success in diverse fields, including material science [28], owing to its flexibility, generalization capability, and robustness to noise [29–32].

Here, ANFIS is employed to model both the p_T distributions and the entropy per unit rapidity ($d\Omega/dy$) of the aforementioned hadrons. By training the model on experimental data, we aim to reproduce the spectra with high accuracy and extrapolate into unmeasured regions. This data-driven approach complements traditional thermal models by improving predictions of key observables at intermediate energies.

In parallel, we analyze the same p_T spectra using two theoretical frameworks: the Hadron Resonance Gas (HRG) model [33] and the Tsallis distribution [34–38]. While the Tsallis distribution effectively describes much of the p_T range, it shows limitations at higher transverse momentum. The HRG model is therefore used to complement the Tsallis fit and extend coverage across the entire spectrum.

Using both measured and predicted p_T distributions, we calculate $d\Omega/dy$ for each particle species, drawing on methods that incorporate femtoscopic measurements (e.g., HBT correlations) for source radii [10, 16]. Previous works have estimated entropy via dN / dy scaling [39, 40], charged particle multiplicities [41, 42], or direct integration over phase-space distributions [43]. Our hybrid approach combines spectral fits with ANFIS predictions, aiming for improved resolution of entropy behavior near the QCD critical region.

The structure of the paper is as follows: section 2 introduces the theoretical and simulation models used. section 3 presents the results and discussion. Conclusions and outlook are summarized in section 4.

2. The used models

In section 2, we present the application of the Adaptive Neuro-Fuzzy Inference System (ANFIS) simulation model [28] for generating and predicting the transverse momentum (p_T) spectra of particles π^{+}, π^{-}, K^{+}, K^{-}, p, and $\bar{p}$ produced in Au–Au collisions at $\sqrt{s_{NN}} = 7.7$ and 11.5 GeV. In addition, we describe the use of two thermal models-the Hadron Resonance Gas (HRG) model and the Tsallis distribution-to fit both the experimental and ANFIS-predicted p_T spectra and to estimate the corresponding entropy per unit rapidity ($d\Omega/dy$) for the same particle species.

2.1. ANFIS model

The Adaptive Neuro-Fuzzy Inference System (ANFIS) is a widely adopted hybrid artificial intelligence (AI) model that integrates the learning capabilities of artificial neural networks (ANNs) with the reasoning of fuzzy logic (FL), enabling effective modeling of complex nonlinear systems [29, 44, 45]. ANFIS uses a hybrid learning algorithm to optimize parameters based on training data, combining the strengths of both AI methods.

Two main types of ANFIS architectures exist: Mamdani and Takagi–Sugeno. The Mamdani method utilizes linguistic rules from human expertise and outputs fuzzy sets, making it suitable for expert systems such as diagnostics. In contrast, the Takagi–Sugeno model uses constant or linear output functions and applies weighted averaging for defuzzification, making it more computationally efficient [30, 46].

In this study, the Takagi–Sugeno ANFIS structure is used due to its efficiency and suitability for modeling hadronic spectra. Its transparent rule-based framework makes it ideal for interpreting physics-related outputs, in contrast to black-box deep neural networks. Moreover, ANFIS is well suited to sparse datasets such as those from $\sqrt{s_{NN}} = 7.7$ and 11.5 GeV collisions, where deep learning methods may overfit. Its fast convergence and flexibility make ANFIS ideal for capturing the nonlinear dynamics in p_T spectra and entropy predictions.

The ANFIS architecture is composed of five layers: fuzzification, rule, normalization, defuzzification, and output. Figure 1 shows the general ANFIS structure [31, 32, 47, 48].

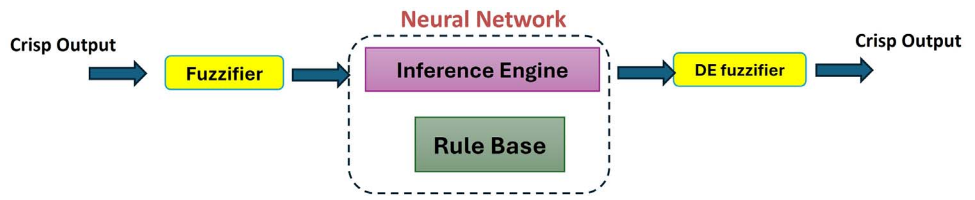

Figure 1. Conceptual illustration of the Adaptive Neuro-Fuzzy Inference System (ANFIS) as a hybrid artificial intelligence technique, integrating fuzzy logic with neural network learning for nonlinear system modeling.

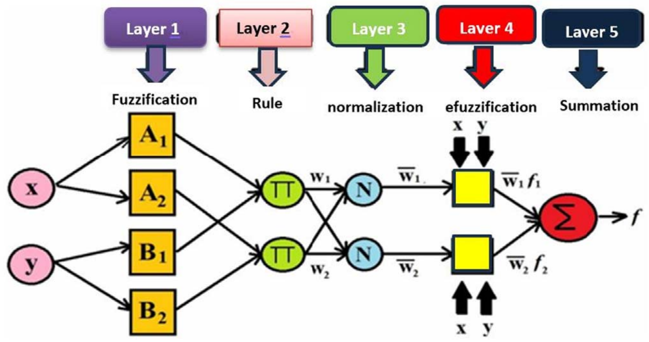

Figure 2. Schematic architecture of a five-layer ANFIS model. Each layer performs a distinct operation, including fuzzification, rule evaluation, normalization, defuzzification, and output summation.

The membership functions form fuzzy clusters using input data, with the general form:

$$\mu A_i(x) = \text{gbellmf}(x;\, a,\, b,\, c) = \frac{1}{1 + \left|\frac{x-c}{a}\right|^{2b}}, \tag{1}$$

where a, b, and c are premise parameters, and $\mu(x)$, $\mu(y) \in [0, 1]$ are membership degrees. Each layer in ANFIS carries out a specific role:

$$O_i^1 = \mu A_i(x), \tag{2}$$

$$O_i^2 = w_i = \mu A_i(x) \cdot \mu B(y), \tag{3}$$

where $i = 1, 2$ denotes the rule index.

The normalization layer outputs:

$$O_i^3 = \bar{w}_i = \frac{w_i}{w_1 + w_2 + w_3}, \tag{4}$$

The defuzzification layer evaluates:

$$O_i^4 = \bar{w}_i f_i = \bar{w}_i (p_i x + q_i y + r_i), \tag{5}$$

where $\{p_i, q_i, r_i\}$ are consequent parameters. The final layer computes the output as:

$$O_i^5 = \sum_i \bar{w}_i f_i = \frac{\sum_i w_i f_i}{\sum_i w_i}. \tag{6}$$

The entire ANFIS computation process is shown in figures 2 and 3.

2.2. ANFIS model configuration

Each ANFIS model consists of five layers and was trained to predict the invariant yield defined as:

$$\frac{1}{N_{\text{evt}}} \frac{d^2 N}{dp_T\, dy}.$$

Inputs to the model include $\sqrt{s}$, p_T, and centrality. Triangular membership functions (trimf) were used for inputs, while a linear function was adopted for outputs. The hybrid learning method combined backpropagation and least-squares optimization to iteratively adjust both premise and consequent parameters.

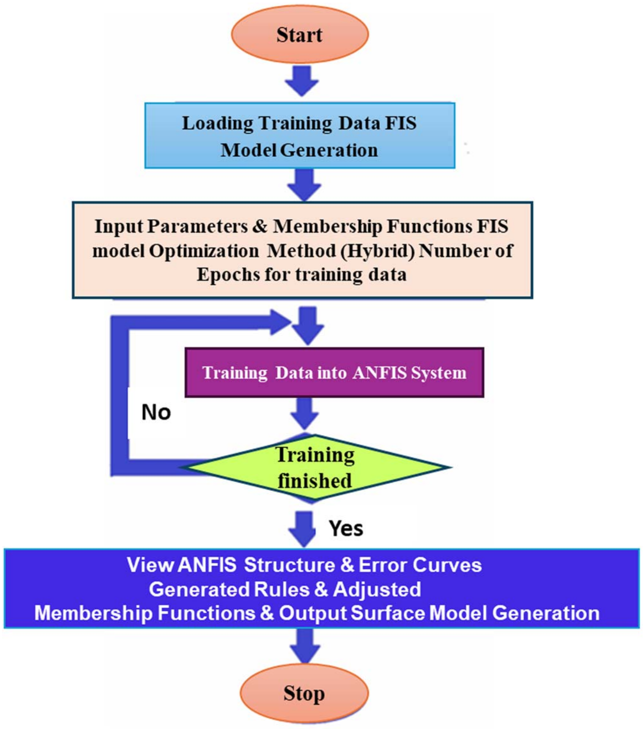

Figure 3. Flowchart outlining the ANFIS processing pipeline used for modeling the p_T spectra and entropy per unit rapidity in heavy-ion collisions.

Table 1. Key ANFIS parameters used for Au–Au collisions at $\sqrt{s} = 7.7$ and 11.5 GeV.

Parameter	Value / Range
Number of nodes	16–44
Training epochs	10–1000
Learning algorithm	Hybrid (Least Squares + Backpropagation)
Input membership functions	Triangular (trimf)
Output membership function	Linear
Fuzzy rules	3–10
Performance metrics	RMSE, MSE

Separate ANFIS networks were trained for each hadron species: π^+, π^-, K^+, K^-, p, and $\bar{p}$. The number of fuzzy rules and membership functions were optimized via a trial-and-error procedure to minimize the root mean squared error (RMSE) and mean squared error (MSE) during training.

The selected configuration parameters used during training - including node counts, learning algorithm, and number of rules - are summarized in table 1. These settings were chosen to balance computational efficiency with prediction accuracy and ensure robust generalization, especially in regions with limited experimental data.

These configurations ensure the model is computationally efficient, generalizes well, and enables extrapolation in sparse regions of the p_T spectrum.

2.3. $d\Omega/dy$ based on the particle momentum spectra p_T

The value of $d\Omega/dy$ (entropy density per unit rapidity) is calculated based on the final phase-space density $f(p, r, t_f)$ at the freeze-out time t_f. The observed spectra reflect only the final momenta p of the particles [16]. Correlations are required to determine the spatial structure of f, as they reveal the characteristic scales of $f(p, r, t)$ for fixed values of p [16, 49, 50]. It has been proposed that a softer equation of state (EOS), associated with a first-order phase transition to the QGP accompanied by significant latent heat, results in prolonged or extended source sizes [16, 51]. The observation that quark-gluon plasma (QGP) models successfully reproduce particle spectra but tend to overestimate the sizes of emission sources [52–58] suggests that the entropy at NICA energies may be lower than that predicted for a QGP.

In this context, we determine $d\Omega/dy$ for hadrons such as $\pi^+, \pi^-, K^+, K^-, p$, and $\bar{p}$ at freeze-out by analyzing the particle yields, transverse momentum spectra, and source sizes in central Au–Au collisions at NICA energies of $\sqrt{s_{NN}} = 7.7$ and 11.5 GeV. Making a comparison between the calculated values of $d\Omega/dy$ for the mentioned particles and those of the early-stage partonic medium helps address critical questions regarding the initial conditions of the collisions and the thermalization of partonic degrees of freedom [16].

Within the framework of Landau quasi-particle, the entropy is expressed as [10, 16, 50, 59]

$$\Omega = (2I+1)\int \frac{d^3r d^3p}{(2\pi)^3}[-f\ln f \pm (1\pm f)\ln(1\pm f)] \approx (2I+1)\int \frac{d^3r d^3p}{(2\pi)^3}[-f\ln f \pm (1\pm f)\ln(1\pm f)], \quad (7)$$

where $(-)+$ sign represents (fermions) bosons. The term $2I+1$ corresponds to the spin-degeneracy of the considered particles. $f \ll 1$ within the classical limit, contributions from f^2 and higher-order terms in f are negligible. The classical approximation holds for any particles, with the exception of pions. In case of pions, f^2 accounts for less than 3% of the total contribution.

For a three-dimensional Gaussian density profile in coordinate space, the single-particle phase-space distribution function at or after freezeout at any time t is [16]

$$f(p, r, t) = f_{max}(p)\exp(-\frac{x^2}{2D_x^2} - \frac{y^2}{2D_y^2} - \frac{z^2}{2R_D^2}), \quad (8)$$

where D_x, D_y, and D_z are depending on p. Since particle spectra are derived by integrating the phase-space distribution function, the maximum value $f_{max}(p)$ and the full distribution $f(p, r, t)$ could be calculated from the measured spectra and radii parameters as

$$\frac{dN}{d^3p} = (2I+1)\int \frac{d^3r}{(2\pi)^3} f(r, p), \quad (9)$$

$$f_{\max}(p) = \frac{(2\pi)^3}{(2I+1)}\frac{dN}{d^3p}\frac{1}{D^3}, \quad (10)$$

where $D^3 = D_x . D_y . D_z$. Chemical equilibration is not considered, as the relations not incorporate chemical potentials or temperature. In contrast, the phase-space densities and consequently the entropy values-are functions of the particle spectra and source dimensions, which are experimentally accessible quantities.

Two-particle correlations are examined in the Longitudinally Co-Moving System (LCMS), where the total longitudinal momentum for each pair of particles is equal to zero ($p_{z,1} + p_{z,2} = 0$GeV/c) [52–58]. To extract femtoscopic radii, the measured correlation functions are fitted to the following form [52–58]:

$$C(K, q) = \frac{P(k_1, k_2)}{P(k_1)P(k_2)} = 1 + \exp(-q_0^2 D_0^2 - q_s^2 D_s^2 - q_l^2 D_l^2), \quad (11)$$

where $q = k_1 - k_2$ and $K = (k_1 + k_2)/2$.

The Gaussian widths in the LCMS frame of equation (11) is connected to the source radii by a factor $\Gamma = \sqrt{m^2 + p_T^2}/m$ in the two-particle correlation rest frame. The densities of phase-space distribution are depended on the product of the three radii as [10, 16]

$$D_{\rm inv}^3 \approx \Gamma D_{\rm out} D_{\rm side} D_{\rm long}, \quad (12)$$

The values of both $D_{\rm inv}$ and $D_{\rm out}$, $D_{\rm side}$, $D_{\rm long}$ that estimated from two-pion correlations in Au-Au nuclear collisions at $\sqrt{s} = 7.7$ and 11.5 GeV are published in [52–58].

Using equation (7), $d\Omega/dy$ is obtained by substituting the radii in equation (10) [10] as

$$\frac{d\Omega}{dy} = \int dp_T 2\pi p_T E\frac{d^3N}{d^3p}\left(\frac{5}{2} - \ln F \pm \frac{F}{2^{5/2}} - \frac{F^2}{2\times 3^{5/2}} \pm \frac{F^3}{3\times 4^{5/2}}\right), \quad (13)$$

where the distribution function of phase space, F, is defined as [10]

$$F(p) = \frac{1}{m}\frac{(2\pi)^{3/2}}{2I+1}\frac{1}{D_{\rm inv}^3(m_{\rm T})}E\frac{d^3N}{d^3p}. \quad (14)$$

To calculate $d\Omega/dy$, we extrapolated the observed spectra, $E\frac{d^3N}{d^3p}$, at $p_T = 0$. For this reason, We confronted the p_T spectra to two different fitting functions deduced from two theoretical models namely; HRG and Tsallis.

The fitting function used for the HRG model is given below [60]

$$\frac{1}{2\pi p_T}\frac{d^2N}{dydp_T} = \frac{Vg_i m_T}{(2\pi)^3}\left[\exp\left(\frac{m_T - \mu_i}{\mathrm{T}}\right) \pm 1\right]^{-1}. \quad (15)$$

where V, μ, and T are the parameters of the statistical fit.

The fitting function considered for the Tsallis distribution is defined as [34, 35]

$$\frac{1}{p_T}\frac{d^2N}{dp_T\,dy}\bigg|_{y=0} = \frac{dN}{dy}\bigg|_{y=0}\frac{m_T}{T}\frac{(2-q)(3-2q)}{(2-q)m_0^2 + 2m_0T + 2T^2}\left[1 + (q-1)\frac{m_0}{T}\right]^{\frac{1}{q-1}}$$
$$\times\left[1 + (q-1)\frac{m_T}{T}\right]^{-\frac{q}{q-1}}. \quad (16)$$

The parameters of the statistical fit are represented by dN/dy, T, and q.

In this work, a hybrid fitting strategy is applied to the transverse momentum (p_T) spectra, where the Tsallis distribution describes the low-p_T region, and the Hadron Resonance Gas (HRG) model fits the intermediate to high-p_T domain. This combination was chosen based on fitting performance: Tsallis captures the exponential behavior at low p_T, while HRG provides a better thermal description at higher momenta.

To connect the two models, a transition point is selected based on the bin-averaged midpoint between the last data point accurately described by Tsallis and the first better fitted by HRG. This point minimizes any discontinuity and is indicated by a vertical line in the plots.

The entropy per unit rapidity ($d\Omega/dy$) is calculated by integrating the entropy density across the full p_T range. The integration includes the measured region using the combined fit, extrapolations at low p_T using Tsallis, and at high p_T using HRG. This approach ensures physical consistency while respecting the validity range of each model.

Although this piecewise method introduces some model dependence, I report the transition points and entropy contributions clearly to maintain transparency and reproducibility. Future extensions may consider smoother interpolations or unified formalisms derived from first principles.

3. The results

This work presents the calculated values of the transverse momentum spectra, $E\frac{d^3N}{d^3p}$, and the entropy per unit rapidity, $d\Omega/dy$, for central Au–Au collisions at the planned NICA accelerator energies of $\sqrt{s_{NN}} = 7.7$ and 11.5 GeV [18, 19].The ANFIS simulation model has the capability to predict values that have not yet been measured. The ANFIS model was trained using 70% of the available experimental data for the transverse momentum spectra, $E\frac{d^3N}{d^3p}$, of hadrons including $\pi^+, \pi^-, K^+, K^-, p$, and $\bar{p}$ at $\sqrt{s} = 7.7$ and 11.5 GeV, respectively. The validation of the ANFIS model was performed by testing its ability to predict experimental values of $E\frac{d^3N}{d^3p}$ for the considered particles at the specified energies. The results obtained from the ANFIS model were compared with the corresponding experimental data for the considered particles. The simulated results of $E\frac{d^3N}{d^3p}$ were used as input data to calculate $d\Omega/dy$ for the considered particles.

3.1. The results of $E\frac{d^3N}{d^3p}$ and $d\Omega/dy$ from Au-Au collision at $\sqrt{s}$=7.7GeV

We estimated the transverse momentum distributions of hadrons, including $\pi^+, \pi^-, K^+, K^-, p$, and $\bar{p}$, produced in Au–Au collisions at $\sqrt{s} = 7.7$ GeV using the ANFIS simulation model [29–32]. The calculated results are compared with the experimental data [18, 19] for the considered particles. The simulated values of $E\frac{d^3N}{d^3p}$ obtained from the ANFIS model are used as input to calculate $d\Omega/dy$. Additionally, the source radii of the identified particles are taken from [52–58]. The ANFIS procedure used to calculate the transverse momentum spectra (p_T) of the identified particles from Au–Au collisions at $\sqrt{s} = 7.7$ GeV is summarized in table 2. This procedure employs a supervised learning algorithm based on the input/output experimental data. The ANFIS model is constructed

using the experimental data as inputs. It consists of six networks, each constructed to carry out the calculation process for a different particle species. Each network is defined by the type and number of membership functions (MFs) used for both inputs and outputs. The networks used in this study consist of three input parameters: $\sqrt{s}$, p_T, and centrality; and one output quantity, $\frac{1}{N_{\rm evt}}\frac{d^2N}{dy\,dp_T}$.

The input variables used for the ANFIS model were selected based on their physical relevance to hadron production in relativistic heavy-ion collisions, as well as their statistical connection to the target output.

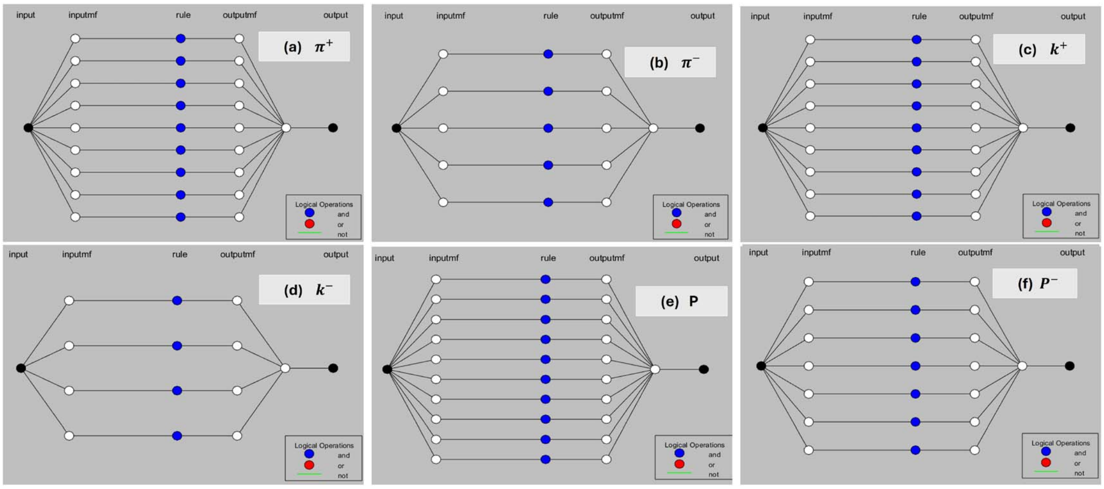

Figure 4. MATLAB-generated ANFIS architectures for the considered hadrons: (a) π^+, (b) π^-, (c) K^+, (d) K^-, (e) p, and (f) $\bar{p}$.

Table 2. ANFIS model input parameters of particles π^+, π^-, k^+, k^-, p, and $\bar{p}$ at $\sqrt{s}$=7.7 GeV.

ANFIS Parameters	The Used Hadrons					
	ANFIS1 π^+	ANFIS2 π^-	ANFIS3 K^+	ANFIS4 K^-	ANFIS5 p	ANFIS6 $\bar{p}$
Inputs	$\sqrt{S}$		p_T(GeV)		Centrality	
$\sqrt{s}$			7.7(GeV)			
Output	$\frac{1}{N_{evt}}\frac{d^2N}{dydp_T}$					
Number of Nodes	40	24	40	20	44	32
Epochs	20	30	60	30	80	20
Number of Linear Parameters	9	5	9	4	10	7
Number of Non-Linear Parameters	27	15	27	12	30	21
Total Number of Parameters	36	20	36	16	40	28
Number of Training data pairs	18	21	13	18	15	8
Number of Fuzzy Rules	9	5	9	4	10	7
ANFIS Start Training	0.0744	0.24089	0.0088	0.0325	0.0234	0.0002
MSE	0.0049	0.029	0.00007	0.001	0.0005	0.00000004
Minimal Training (RMSE)	0.0705	0.1731	0.0088	0.0325	0.0235	0.0002
Type of Membrane Functions (Inputs)			Trimf			
Type of MF (Outputs)			Linear			

Specifically, we used the center-of-mass energy $\sqrt{s_{NN}}$, the transverse momentum p_T, and the collision centrality. The selected input set was found to offer a good compromise between accuracy and physical interpretation, which is important for the ANFIS hybrid AI model.

Since the output values vary between different particle species, we trained each ANFIS network independently for every particle. The input data were used to train and evaluate the six proposed models (ANFIS 1 to ANFIS 6), each corresponding to a specific particle: π^+, π^-, K^+, K^-, p, and $\bar{p}$ at $\sqrt{s}\ = 7.7$ GeV. The membership functions in the models were selected based on a trial-and-error approach to ensure optimal performance during training. The optimal ANFIS network was selected by retraining the model multiple times with different configurations and choosing the one that achieved the lowest training error. Additionally, the number of training epochs was adjusted to further minimize the training error. The model was further trained using the hybrid learning algorithm with zero error tolerance to ensure precise convergence. The ANFIS models were constructed using triangular membership functions (Trimf) for the inputs in ANFIS 1 through ANFIS 6, whereas a linear function was applied to the output layer. The Trimf method does not lead to overfitting and results in the lowest RMSE. It allows for easy interpretation and visualization of the inputs through fuzziness, which enhances the model's transparency. Trimf also provides faster training and evaluation, especially when working with large datasets, offering a good balance between accuracy and simplicity. Figure 4 shows the architectures of the best-trained ANFIS 1 to ANFIS 6 models for the six hadrons: (a) π^+, (b) π^-, (c) K^+, (d) K^-,

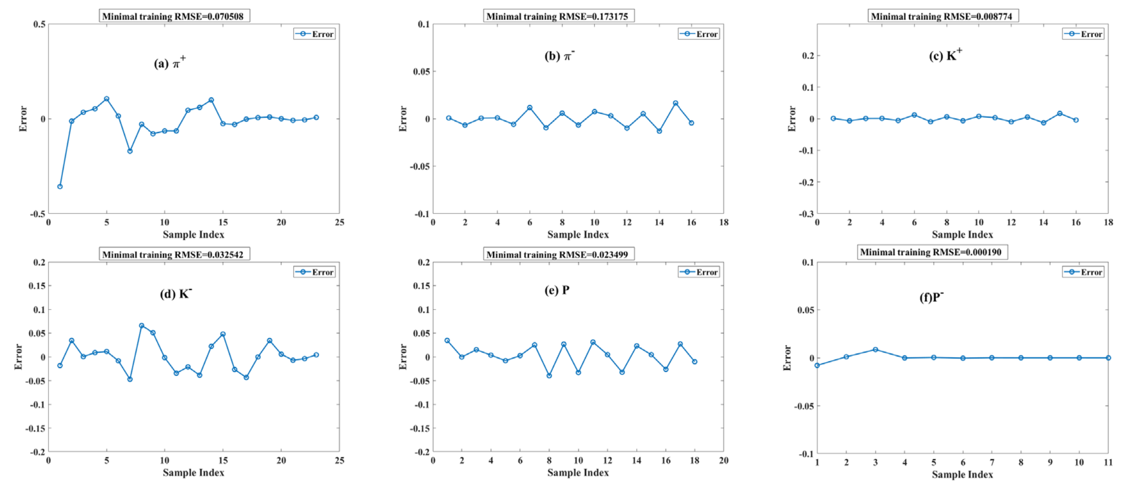

Figure 5. Minimal *RMSE* values obtained for the hadrons (a) π^+, (b) π^-, (c) k^+, (d) k^-, (e) p, and (f) $\bar{p}$ using the ANFIS model.

(e) p, and (f) $\bar{p}$, respectively. Using the proposed ANFIS 1–ANFIS 6 models [61, 62], we achieved the lowest Mean Squared Error (MSE) values for each particle.

The optimal performance of each ANFIS network is evaluated using the error metrics: instantaneous error e_t, mean error $\bar{e}_t$, mean squared error (MSE), root mean squared error (RMSE), and standard deviation error (Std), all calculated from the training dataset and defined in equations (17)–(21) [63].

$$e_t = Values_{predicted} - Values_{measured}, \tag{17}$$

$$\bar{e}_t = e_t/n, \tag{18}$$

$$MSE = (1/n)\sum_{t=1}^{n} e_t^2, \tag{19}$$

$$RMSE = (1/n)\sqrt{\sum_{t=1}^{n} e_t^2}, \tag{20}$$

$$Std = \sqrt{\sum_{t=1}^{n} \frac{e_t^2}{n} - 1}. \tag{21}$$

where n represents the number of points for experimental data. A mean squared error (MSE) value approaching zero indicates that the discrepancy between the ANFIS network output and the target output is minimal, reflecting high prediction accuracy. When the MSE value is zero, it means there's no difference or error between the network's output and the desired result. The RMSE value shows how closely the outputs are correlated. The strong agreement between the proposed model and the experimental data encourages us to predict some p_T values for the considered particles at $\sqrt{s} = 7.7$ GeV. These positive results open the door for deeper investigations and predictions of key physical quantities, especially in areas not yet explored experimentally. The RMSE values obtained for the particles (a) π^+, (b) π^-, (c) k^+, (d) k^-, (e) p, and (f) $\bar{p}$ are displayed in figure 5.

As shown in figure 5, most points lie very close to the zero-error line, which confirms the effectiveness of the applied model. For all particles considered, the RMSE values are very small, indicating excellent agreement between the ANFIS model predictions and the experimental data. The best training results for all particles are clearly illustrated in figure 6. The RMSE values were obtained after epochs 20, 30, 60, 30, 80, and 20 for particles (a) π^+, (b) π^-, (c) k^+, (d) k^-, (e) p, and (f) $\bar{p}$, respectively. These results are presented alongside the suggested fuzzy rules in table 2. The minimal training MSE did not exceed 10^{-1} within the range of epochs from 20 to 80 for the particles mentioned. The membership functions (inputs) used in the ANFIS model are of the Trimf type, with a linear function applied in the output layer for all particles. This shows that the best ANFIS networks follow the Takagi-Sugeno type and involve multiple parameters, as detailed in table 2. Additionally, these networks utilize the weighted average (Wtaver) method as the defuzzification technique during training.

In order to calculate $\frac{d\Omega}{dy}$, we extrapolated the measured particle spectra of π^+, π^-, k^+, k^-, p, and $\bar{p}$ [18, 19] to $p_T = 0$. The values of both observed and simulated particle transverse momentum spectra, p_T, are fitted using two functions from different theoretical models: the HRG model [33] and the Tsallis distribution [34, 35]. Both approaches successfully described the entire range of the p_T spectra. Additionally, $\langle p_T \rangle$ is sensitive to the fitting range selected for the p_T spectra. Variations in the $\langle p_T \rangle$ values resulting from the considered fitting ranges are incorporated into the overall systematic uncertainties [64]. The results presented here represent the combined

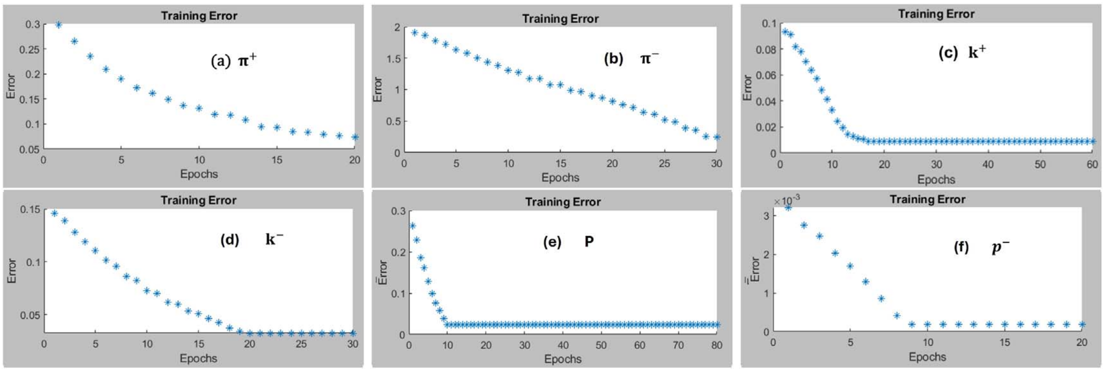

Figure 6. Best training results for the hadrons (a) π^+, (b) π^-, (c) k^+, (d) k^-, (e) p, and (f) $\bar{p}$.

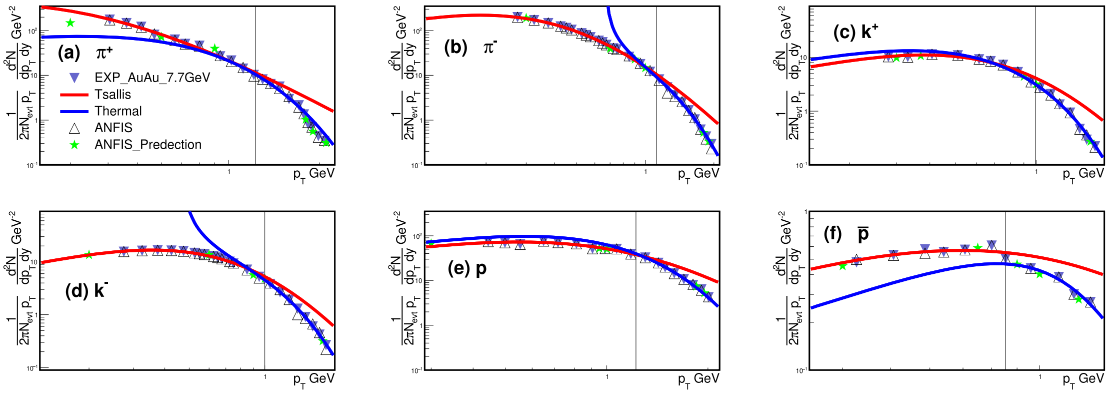

Figure 7. The particle momentum spectra [18, 19, 64], represented by blue closed inverse triangle symbols, of the mentioned hadrons (a) π^+, (b) π^-,(c) k^+, (d) k^-, (e) p, and (f) $\bar{p}$ is confronted to the statistical fits from Tsallis distribution, appeared by red solid line, using equation (16) and the HRG model, appeared by solid blue line, using equation (15) at $\sqrt{s} = 7.7$GeV. A separating line, appeared by solid black line, is made between both HRG and Tsallis models. The observed values and the two statistical fit functions are confronted to the one calculated from the ANFIS model, appeared by black triangle symbols. The prediction of some values by ANFIS model is shown by red color star symbols. The uncertainties are statistical and systematic added in quadrature.

systematic and statistical uncertainties added in quadrature, with the statistical uncertainties being negligibly small. The comparison between the simulated and measured transverse momentum spectra, p_T, fitted using both the HRG and Tsallis models [34, 35], is clearly presented in figure 7 for the particles (a) π^+, (b) π^-, (c) k^+, (d) k^-, (e) p, and (f) $\bar{p}$. Figure 7 illustrates the reason for using two fitting functions: the Tsallis distribution effectively describes the low-p_T region of the particle spectra, while the HRG model fits the high-p_T region. We summarized the fitting parameters of the HRG and Tsallis models in tables 3 and 4, respectively, comparing them with both the observed and simulated values.

A detailed comparison between the ANFIS, Tsallis, and HRG models reveals noticeable differences in both the shape and extrapolation behavior of the transverse momentum spectra. While all models show good agreement in the mid-p_T region, the ANFIS predictions tend to better capture the curvature of the spectra at low and high p_T, particularly for heavier hadrons such as protons and antiprotons. This improved performance is attributed to ANFIS's ability to learn nonlinear features from the data without assuming a fixed functional form.

The differences between models also translate into variations in the estimated entropy per unit rapidity ($d\Omega/dy$). For instance, in the high-p_T region where data are sparse, the HRG model often underestimates contributions to the entropy compared to ANFIS, which is capable of extrapolating more smoothly based on learned data patterns. These discrepancies highlight the model dependence of entropy calculations, especially when integrating over extended p_T ranges.

Uncertainty in the ANFIS predictions arises primarily from the limited size and coverage of the training dataset, as well as from the model's sensitivity to input parameter tuning. While the current work focuses on central predictions, we acknowledge the need for formal uncertainty quantification methods-such as ensemble modeling or input perturbation-which will be addressed in future studies. Despite this, the consistent performance of ANFIS across different particle species suggests it is a robust tool for modeling hadronic observables at intermediate energies.

Table 3. The statistical fitting parameters of p_T spectra as comparing the observed values [18, 19] to the HRG model, equation (15), and the Tasllis distribution, equation (16), of particles π^+, π^-, k^+, k^-, p, and $\bar{p}$ at $\sqrt{s}$=7.7GeV.

Hadron	Tsallis			HRG approach			χ^2 /dof
	dN/dy	T_{Ts}GeV	q	V fm^3	T_{th}GeV	μGeV	
π^+	167.313 ± 17.93	0.044936 ± 0.0052	1.19401 ± 0.1193	79.678 ± 88.9885	0.2316 ± 0.1822	6.15425 ± 1.3801	0.0475/9
π^-	105.179 ± 11.43	0.07284 ± 0.0082	1.1379 ± 0.1521	534.078 ± 144.738	0.5283 ± 0.03257	8.253 ± 0.2705	12.269/14
K^+	9.47079 ± 0.8951	0.12023 ± 0.0142	1.10967 ± 0.1692	11312 ± 5224.5	1.0965 ± 0.0597	10.1193 ± 0.3552	11/6
K^-	13.317 ± 1.5261	0.1052 ± 0.0129	1.11337 ± 0.1193	5251.68 ± 1016.59	0.9282 ± 0.0234	9.8205 ± 0.1489	236.085/12
p	90.9097 ± 10.03	0.0914 ± 0.0098	1.15275 ± 0.1357	6256.7 ± 1312	0.5989 ± 0.3211	7.5465 ± 1.3412	0.0169/7
$\bar{p}$	1.1319 ± 0.1472	0.0964 ± 0.001251	1.2421 ± 0.1421	6.9859 ± 2.6106	0.3982 ± 0.0851	5.1304 ± 0.4311	3.0475/4

Table 4. Similar to that of table 3 but the fitting parameters are obtained from comparing the used theoretical models with ANFIS simulation model.

Hadron	Tsallis			HRG approach			χ^2 /dof
	dN/dy	T GeV	q	V fm^3	T GeV	μGeV	
π^+	168.213 ± 17.054	0.04562 ± 0.0042	1.1825 ± 0.109	65.516 ± 45.7421	0.3581 ± 0.0375	5.8371 ± 1.0584	0.0573/13
π^-	103.821 ± 12.315	0.0813 ± 0.0079	1.1251 ± 0.106	526.754 ± 156.213	0.4917 ± 0.00532	7.9721 ± 0.2617	13.765/14
K^+	9.2831 ± 0.8976	0.1391 ± 0.0147	1.1254 ± 0.137	11761 ± 6731.23	1.1210 ± 0.0421	9.9421 ± 0.5217	18.23/7
K^-	14.098 ± 0.1398	0.1161 ± 0.0215	1.11487 ± 0.1263	5743.31 ± 1100.51	0.8931 ± 0.02931	8.6512 ± 0.1621	255.917/16
p	83.7281 ± 9.792	0.08421 ± 0.00986	1.1376 ± 0.1402	6735.94 ± 1218	0.6815 ± 0.4174	6.9854 ± 1.2043	0.0205/8
$\bar{p}$	1.1174 ± 0.1402	0.1021 ± 0.0241	1.1951 ± 0.1302	5.3421 ± 1.9581	0.4261 ± 0.0681	6.461 ± 0.3761	4.871/5

Table 5. The calculated values of the entropy-per-rapidity $d\Omega/dy$ from Au-Au nuclear collisions at $\sqrt{s}$=7.7GeV using the HRG model, Tsallis distribution, and the ANFIS model.

Hadron	$d\Omega/dy$	$d\Omega/dy$ Including Tsallis	$d\Omega/dy$ Including (HRG+Tsallis)	$d\Omega/dy$ obtained by ANFIS
π^+	294.413 $\pm$ 44.5	683.009 $\pm$ 104.0	684.359 $\pm$ 110.7	679.241 $\pm$ 51.6
π^-	302.611 $\pm$ 36.7	482.864 $\pm$ 91.0	483.56 $\pm$ 98.1	491.54 $\pm$ 43.2
K^+	34.23 $\pm$ 7.6	56.35 $\pm$ 13.5	68.664 $\pm$ 15.5	67.96 $\pm$ 12.3
K^-	81.0268 $\pm$ 8.1	94.0706 $\pm$ 11.8	94.8378 $\pm$ 14	95.648 $\pm$ 13.1
p	455.854 $\pm$ 61.3	539.251 $\pm$ 97.0	549.517 $\pm$ 114.4	538.745 $\pm$ 52.7
$\bar{p}$	5.02324 $\pm$ 1.0	6.1298 $\pm$ 1.52	7.0174 $\pm$ 1.81	9.3721 $\pm$ 1.65

Table 6. ANFIS model input parameters of particles $\pi^+, \pi^-, k^+, k^-, p$, and $\bar{p}$ at $\sqrt{s}$=11.5GeV.

ANFIS Parameters	The Used Hadrons					
	ANFIS1 π^+	ANFIS2 π^-	ANFIS3 K^+	ANFIS4 K^-	ANFIS5 p	ANFIS6 $\bar{p}$
Inputs	$\sqrt{S}$		p_T(GeV)		Centrality	
$\sqrt{s}$			11.5(GeV)			
Output	$\frac{1}{N_{evt}}\frac{d^2N}{dydp_T}$					
Number of Nodes	20	24	20	20	16	16
Epochs	50	30	10	1000	30	30
Number of Linear Parameters	4	5	4	4	3	3
Number of Non-Linear Parameters	12	15	12	12	9	9
Total Number of Parameters	16	20	16	16	12	12
Number of Training data pairs	21	21	20	16	22	18
Number of Fuzzy Rules	4	5	4	4	3	3
ANFIS Start Training	0.5429	0.2636	0.0867	0.0164	0.0834	0.0036
MSE	0.294	0.03	0.0057	0.0003	0.0069	0.000012
Minimal Training (RMSE)	0.5429	0.1734	0.0759	0.0164	0.0834	0.0036
Type of Membrane Functions (Inputs)			Trimf			
Type of MF (Outputs)			Linear			

The calculated values of $\frac{d\Omega}{dy}$ from Au-Au collisions at $\sqrt{s} = 7.7$ GeV using the HRG model, Tsallis distribution, and ANFIS simulation for particles $\pi^+, \pi^-, k^+, k^-, p$, and $\bar{p}$ are presented in table 5. This table also highlights the impact of the fitting functions used in the HRG and Tsallis models on the estimated $d\Omega/dy$. A comparison with the ANFIS results shows good agreement among all the proposed models.

Table 5 shows that the values of $\frac{d\Omega}{dy}$ obtained from the statistical fits of both the HRG and Tsallis models are in better agreement with those estimated by the ANFIS model. The good agreement between the theoretical models (HRG and Tsallis) and the ANFIS simulation in estimating $\frac{d\Omega}{dy}$ supports the use of the ANFIS model to predict values at the energies relevant to future NICA facilities.

The entropy per rapidity values calculated using the Tsallis, HRG, and ANFIS models show a generally good level of agreement, especially for the lighter hadrons such as pions and kaons. The Tsallis distribution provides a reliable description in the low-to-intermediate p_T region, while the HRG model complements it well at higher p_T, and their combination captures the full spectrum effectively. The ANFIS predictions follow the same trend and stay within the uncertainty range of the other methods, reinforcing its validity as a data-driven approach. The uncertainties, derived from the propagation of fit parameter errors, give a clearer picture of the model stability and indicate where extrapolations contribute most to the final entropy estimates.

3.2. The results of $E\frac{d^3N}{d^3p}$ and $d\Omega/dy$ from Au-Au collisions at $\sqrt{s}$=11.5GeV

We trained the proposed ANFIS simulation model [29–32] to estimate the transverse momentum spectra p_T of particles $\pi^+, \pi^-, k^+, k^-, p$, and $\bar{p}$ produced in Au-Au collisions at $\sqrt{s} = 11.5$ GeV [18, 19]. The calculated results are compared with the experimental data of the considered particles [18, 19]. The simulated values of $E\frac{d^3N}{d^3p}$ obtained from the ANFIS model are then used as input to calculate $\frac{d\Omega}{dy}$. Additionally, the source radii values for the considered particles were taken from [52–58]. The steps followed in the ANFIS simulation to calculate the transverse momentum spectra p_T of these particles produced in Au-Au collisions at $\sqrt{s} = 7.7$ GeV are summarized in table 6. This process involves a supervised learning algorithm, which depends on the input/output experimental data used during training. The ANFIS model is developed based on the experimental data

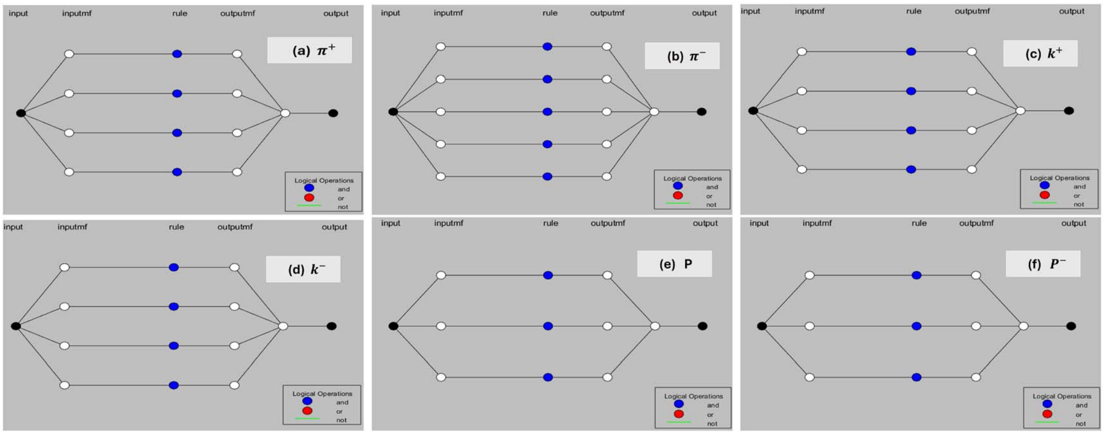

Figure 8. Similar to that of figure 4 but for hadrons (a) π^+, (b) π^-,(c) k^+, (d) k^-, (e) p, and (f) $\bar{p}$ at $\sqrt{s}$=11.5GeV.

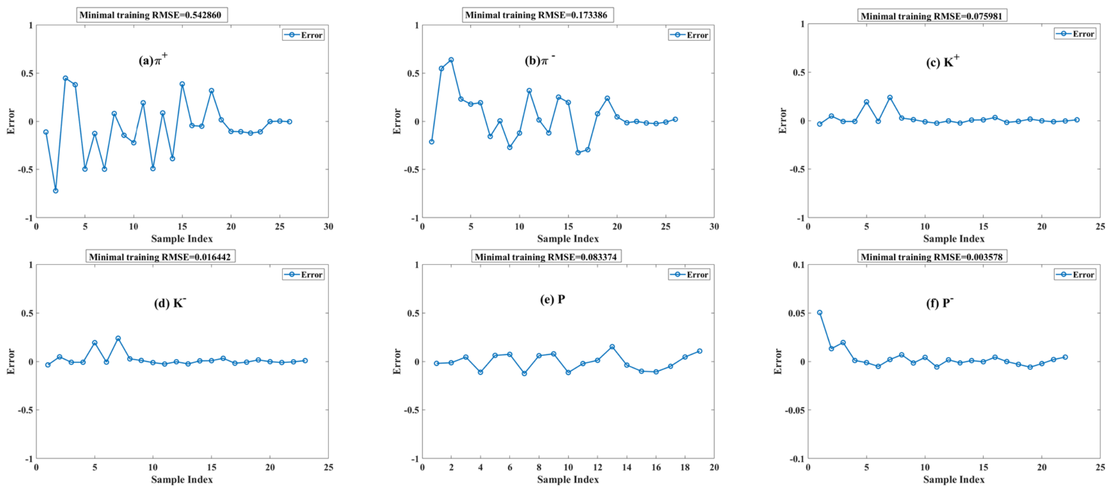

Figure 9. Similar to that of figure 5 but for hadrons (a) π^+, (b) π^-,(c) k^+, (d) k^-, (e) p, and (f) $\bar{p}$ at $\sqrt{s}$=11.5GeV.

as inputs. It comprises six networks, each constructed to model one of the six different particles. Each network is characterized by the type and number of membership functions (MFs) used for both the input and output layers. The constructed networks consist of three input parameters: $\sqrt{s}$, p_T, and centrality, with one output value, $\frac{1}{N_{\text{evt}}}\frac{d^2N}{dy\, dp_T}$. Due to the variation among particles, the output values differ; therefore, each network was trained independently. The input data were used to train and evaluate the six proposed models (ANFIS 1-ANFIS 6), corresponding to the particles π^+, π^-, k^+, k^-, p, and $\bar{p}$ at $\sqrt{s}\ =\ 7.7$ GeV. The membership functions of the models were determined through an iterative trial-and-error process. The best ANFIS network, identified by the lowest training error, is selected after multiple retraining cycles using different configurations within the model. Additionally, the number of training epochs can be adjusted to further minimize the training errors. The procedure was further refined using the hybrid learning algorithm, with the goal of achieving zero error tolerance. The ANFIS models were constructed using the Trimf membership function for the input variables in ANFIS 1 through ANFIS 6, while a linear function was applied in the output layer. Figure 8 illustrates the architectures of the top-trained ANFIS 1-ANFIS 6 models for particles (a) π^+, (b) π^-, (c) k^+, (d) k^-, (e) p, and (f) $\bar{p}$, respectively. Using the models ANFIS 1 through ANFIS 6 [61], the best Mean Squared Error (MSE) values were obtained.

The best performance of the network is evaluated by analyzing the error metrics: instantaneous error e_t, mean error $\bar{e}_t$, Mean Squared Error (MSE), Root Mean Squared Error (RMSE), and standard deviation error (Std), as defined in equations (17–21) [63]. If the MSE coefficient approaches zero, it indicates that the difference between the network output and the target output is negligible. In case the MSE coefficient equals 0, it means there is no error or difference between the desired output and the network output. The RMSE value provides an indication of the degree of agreement between the model outputs and the target values. The obtained values of both *MSE* and *RMSE* for the particles (a) π^+, (b) π^-, (c) k^+, (d) k^-, (e) p, and (f) $\bar{p}$ are presented in figures 9 and 10, respectively.

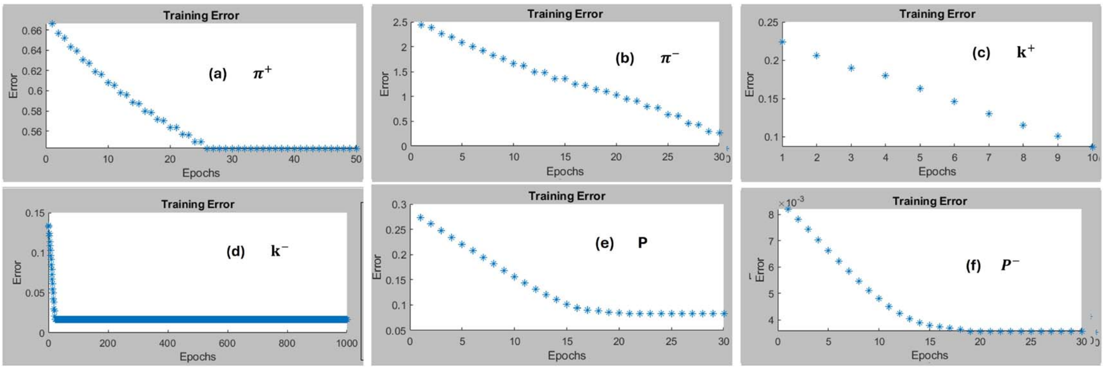

Figure 10. Similar to that of figure 6 but for hadrons (a) π^+, (b) π^-,(c) k^+, (d) k^-, (e) p, and (f) $\bar{p}$ at $\sqrt{s}$=11.5GeV.

As illustrated in figure 9, most points lie very close to the zero-error line, confirming the reliability of the model results. It is clear that the RMSE values for all considered particles are close to each other, indicating excellent agreement between the results of the proposed ANFIS model and the experimental data. The excellent agreement between the ANFIS model and the observed data encourages us to predict p_T values for the mentioned particles at $\sqrt{s} = 11.5$ GeV.

As a result, further investigations and predictions of key physical quantities-especially in regions not yet explored experimentally-can be pursued. The best training results for all defined particles are clearly illustrated in figure 10. The corresponding *RMSE* values were obtained after epochs 50, 30, 10, 1000, 30, and 30 for hadrons (a) π^+, (b) π^-, (c) k^+, (d) k^-, (e) p, and (f) $\bar{p}$, respectively. These results are presented along with all the fuzzy rules used in table 2. The minimal training *MSE* was found to not exceed 10^{-1} within the epoch range of 20 to 80 for the mentioned particles. The membership functions used in the proposed ANFIS model are of the Trimf type for the input layer and linear for the output layer across all particles. It is demonstrated that the optimal ANFIS networks are of the Takagi-Sugeno type, incorporating multiple parameters as detailed in table 6. Additionally, these networks utilize the weighted average (Wtaver) method as the defuzzification technique during the training process.

The estimated values of p_T along with the source radii of the particles π^+, π^-, k^+, k^-, p, and $\bar{p}$ [52–58] are used as input to calculate $\frac{d\Omega}{dy}$.

To achieve this, the measured spectra of particles π^+, π^-, k^+, k^-, p, and $\bar{p}$ [18, 19] were extrapolated down to $p_T = 0$. Both the measured and simulated p_T spectra are fitted using two functions based on different theoretical models: the HRG model [33] and the Tsallis distribution [34, 35]. The two employed models have successfully described the full range of the p_T spectra. A comparison between the simulated and measured p_T spectra, using both the HRG [33] and Tsallis [34, 35] fitting functions, is presented in figure 11 for the particles (a) π^+, (b) π^-, (c) k^+, (d) k^-, (e) p, and (f) $\bar{p}$. Figure 7 illustrates the motivation for employing two fitting functions: the Tsallis distribution provides a better fit for the low-p_T region of the particle spectra, while the HRG model more accurately describes the high-p_T region.

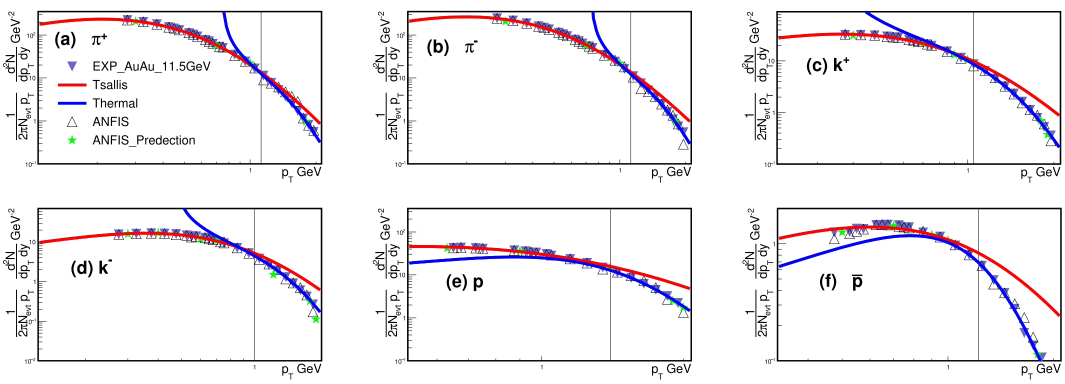

Figure 11. The particle momentum spectra [18, 19, 64], represented by blue closed inverse triangle symbols, of particles (a) π^+, (b) π^-, (c) k^+, (d) k^-, (e) p, and (f) $\bar{p}$ is confronted to the fitting functions of Tsallis distribution, appeared by red solid line, using equation (16) and the HRG model, appeared by solid blue line, using equation (15) at $\sqrt{s} = 11.5$GeV. A separating line, appeared by solid black line, is made between both HRG and Tsallis models. The observed values and the statistical fits of the two approaches are confronted to the one calculated from the ANFIS model, represented by black triangle symbols. The prediction of some values by ANFIS model is shown by red color star symbols. The uncertainties are statistical and systematic added in quadrature.

Table 7. The statistical fitting parameters of p_T spectra as comparing the observed values [18, 19] to the HRG model, equation (15), and the Tasllis distribution, equation (16), of particles π^+, π^-, k^+, k^-, p, and $\bar{p}$ at $\sqrt{s}$=11.5GeV.

Hadron	Tsallis distribution			HRG model			χ^2/dof
	dN/dy	T_{Ts}GeV	q	V fm^3	T_{th}GeV	μGeV	
π^+	120.255 ± 13.45	0.0885 ± 0.0092	1.1142 ± 0.1281	5760 ± 1120.8	0.7759 ± 0.02066	9.7591 ± 0.1608	12.617/14
π^-	130.895 ± 14.95	0.08025 ± 0.0089	1.12615 ± 0.1311	1732.26 ± 415.761	0.6362 ± 0.02686	8.9271 ± 0.2165	8.9477/14
K^+	27.099 ± 2.8345	0.1091 ± 0.0011	1.1146 ± 0.1207	11591 ± 2685.04	0.9519 ± 0.0288	9.7276 ± 0.1689	6.49/11
K^-	12.417 ± 1.3042	0.1142 ± 0.0121	1.11227 ± 0.1192	4251.68 ± 1020.79	0.8282 ± 0.0234	7.9204 ± 0.1267	1.633/12
p	52.847 ± 5.9732	0.1074 ± 0.0119	1.1227 ± 0.1324	44.224 ± 1.079	0.1956 ± 0.0007	1.3014 ± 0.0058	0.0032/4
$\bar{p}$	1.8733 ± 0.1921	0.1374 ± 0.0149	1.1323 ± 0.1294	2.5765 ± 0.4058	0.1871 ± 0.0041	1.2045 ± 0.0366	0.0007/5

Table 8. Similar to that of table 7 but the fitting functions, of both used models, are compared to the ANFIS model.

Hadron	Tsallis			HRG approach			χ^2/dof
	dN/dy	T GeV	q	V fm^3	T GeV	μGeV	
π^+	122.513 ± 12.95	0.07431 ± 0.0082	1.1201 ± 0.1203	6101.516 ± 1240.10	0.6802 ± 0.03021	9.1061 ± 0.1852	13.473/14
π^-	129.912 ± 12.99	0.0839 ± 0.096	1.1273 ± 0.1342	1697.51 ± 510	0.6873 ± 0.0361	7.6721 ± 0.2471	11.2/15
K^+	29.732 ± 3.1073	0.1151 ± 0.0129	1.1201 ± 0.1293	11207 ± 3051.41	1.051 ± 0.0301	8.9051 ± 0.2061	8.51/12
K^-	11.692 ± 1.2972	0.1281 ± 0.0137	1.11729 ± 0.1209	5061.52 ± 1081.21	0.8731 ± 0.02731	8.2076 ± 0.1371	1.976/17
p	55.614 ± 5.9732	0.0975 ± 0.0099	1.1295 ± 0.1392	47.781 ± 1.821	0.2351 ± 0.0050	1.3974 ± 0.0063	0.0051/5
$\bar{p}$	1.8194 ± 0.1972	0.1197 ± 0.0213	1.1283 ± 0.1304	3.1843 ± 0.5732	0.1695 ± 0.0062	1.4631 ± 0.0472	0.0009/6

Table 9. Similar to that of table 5 but at $\sqrt{s}$=11.5GeV.

Hadron	$d\Omega/dy$	$d\Omega/dy$ Including Tsallis	$d\Omega/dy$ Including (HRG+Tsallis)	$d\Omega/dy$ obtained by ANFIS model
π^+	367.699 $\pm$ 42.6	551.197 $\pm$ 78.3	552.579 $\pm$ 89.7	550.98141.3
π^-	377.328 $\pm$ 39.2	581.927 $\pm$ 81.0	583.207 $\pm$ 90.1	590.41 $\pm$ 42.0
K^+	166.343 $\pm$ 19.3	182.602 $\pm$ 26.7	183.851 $\pm$ 32.6	184.16 $\pm$ 13.8
K^-	81.027 $\pm$ 10.8	94.071 $\pm$ 13.4	94.8378 $\pm$ 17.2	93.25 $\pm$ 7.5
p	170.159 $\pm$ 21.5	346.845 $\pm$ 52.4	351.625 $\pm$ 56.6	352.75 $\pm$ 30.2
$\bar{p}$	12.3694 $\pm$ 2.1	15.9256 $\pm$ 2.7	16.123 $\pm$ 3.4	18.75 $\pm$ 1.9

The resulting fitting parameters from both the HRG and Tsallis models are summarized in tables 7 and 8, respectively, where they are compared with both the observed data [18, 19] and the corresponding simulated values.

The calculated values of $\frac{d\Omega}{dy}$ from Au-Au nuclear collisions at $\sqrt{s}\ =\ 11.5$ GeV, obtained using the HRG model, Tsallis distribution, and the ANFIS simulation for particles $\pi^+, \pi^-, k^+, k^-, p$, and $\bar{p}$, are presented in table 9. The fitting parameters of the HRG model and the Tsallis distribution are presented in table 9. We compared the calculated values of $\frac{d\Omega}{dy}$ obtained from the HRG and Tsallis fits with those predicted by the ANFIS model. The comparison shows strong agreement among the models.

At $\sqrt{s_{NN}}\ =\ 11.5$ GeV, the entropy per unit rapidity ($d\Omega/dy$) was evaluated for six hadron species using four approaches: the Tsallis distribution, the HRG model, a hybrid fit combining both, and the ANFIS simulation. The results are summarized in table 9. For instance, in the case of π^+, the Tsallis model yielded 551.2 $\pm$ 78.3, while the HRG model produced a lower value of 367.7 $\pm$ 42.6. Combining the fits across different p_T regions led to an entropy value of 552.6 $\pm$ 89.7, closely aligned with the ANFIS prediction of 551.0 $\pm$ 41.3. Similar consistency is observed across the remaining hadrons, where ANFIS outputs are in excellent agreement with the hybrid model, confirming the robustness of the entropy estimates.

The entropy per unit rapidity serves as a key thermodynamic observable, reflecting the system's microscopic degrees of freedom and evolution at the freeze-out stage. Within the QCD phase diagram, its behavior may offer indirect signals of phase transitions. While a smooth increase in $d\Omega/dy$ with energy is generally expected due to enhanced particle production, non-monotonic behavior may suggest deconfinement or the vicinity of a critical point.

At NICA energies ($\sqrt{s}\ =\ 7.7$ and 11.5 GeV), where the baryon chemical potential is high, the extracted p_T spectra and entropy provide valuable probes of dense QCD matter. Thermal models such as Tsallis and HRG have proven effective in describing the spectra but rely on simplifying assumptions-Tsallis being phenomenological and HRG assuming a chemically equilibrated, non-interacting hadron gas-which may limit their applicability at large μ_B.

The ANFIS framework offers a complementary, data-driven approach capable of learning from experimental trends and making reliable predictions even beyond the measured range. However, its predictive accuracy depends heavily on the quality and extent of its training data. In regions where experimental data are sparse or new physics may emerge, such as near phase boundaries, caution must be exercised when interpreting its outputs [65, 66].

Together, these methodologies enhance our ability to probe the QCD phase structure and contribute meaningfully to the overarching goals of the NICA program, particularly in exploring the behavior of strongly interacting matter under extreme conditions.

4. Conclusions

In this study, we analyzed the transverse momentum (p_T) spectra of particles $\pi^+, \pi^-, k^+, k^-, p$, and $\bar{p}$ produced in Au-Au collisions at the planned NICA energies of $\sqrt{s}\ =\ 7.7$ and 11.5 GeV. The proposed ANFIS simulation model was employed to estimate the p_T distributions. When compared with experimental data, the ANFIS model demonstrated excellent agreement, validating its effectiveness and motivating its use for predicting values in regions beyond current measurements.

The predicted p_T values, along with source size inputs, were used to calculate the entropy per unit rapidity ($d\Omega/dy$). To cover the full p_T range-including the unmeasured low-p_T region-experimental spectra were extrapolated to $p_T = 0$. Both the measured and predicted spectra were fitted using two theoretical models: the Hadron Resonance Gas (HRG) model and the Tsallis distribution. Each model effectively described different parts of the spectra: Tsallis captured the low-p_T region, while HRG performed better at higher p_T. This complementary fitting approach successfully reproduced the full p_T range.

The consistency between the ANFIS model outputs and the experimental data confirms its reliability as a predictive tool. Its success in modeling measured spectra and estimating $d\Omega/dy$ suggests it can be confidently applied to explore critical observables in regions not yet accessible experimentally. This work supports the use of hybrid approaches-combining machine learning and theoretical models-to probe the properties of strongly interacting matter at NICA energies.

Acknowledgments

The authors thank Sergey Nedelko, Evgeni Kolomeitsev, and the Laboratory of Theoretical Physics of JINR for their hospitality and help. The authors are grateful for the support provided by ASRT (the Egyptian Academy for Scientific Research and Technology) through the ASRT-JINR (Joint Institute for Nuclear Research, Dubna, Russia) agreement projects (Call-2023), which facilitated the performance of this work at JINR.

Data availability statement

All data that support the findings of this study are included within the article (and any supplementary files).

References

[1] Braun-Munzinger P, Cleymans J, Oeschler H and Redlich K 2002 *Nucl. Phys. A* **697** 902
[2] Ivanov Y B, Russkikh V N and Toneev V D 2006 *Phys. Rev. C* **73** 044904
[3] Friman B, Norenberg W and Toneev V D 1998 *Eur. Phys. J. A* **3** 165
[4] Cassing W and Bratkovskaya E L 1999 *Phys. Rept.* **308** 65
[5] Blume C 2005 *J. Phys. G* **31** S685
[6] Sorensen A *et al* 2024 *Prog. Part. Nucl. Phys.* **134** 104080
[7] Borsanyi S, Fodor Z, Guenther J N, Parotto P, Pasztor A, Ratti C, Vovchenko V and Wong C H 2025 arXiv:2502.10267
[8] Harris J W and Müller B 2024 *Eur. Phys. J. C* **84** 247
[9] Aoki Y, Endrodi G, Fodor Z, Katz S D and Szabo K K 2006 *Nature* **443** 675
[10] Hanus P, Mazeliauskas A and Reygers K 2019 *Phys. Rev. C* **100** 064903
[11] Busza W, Rajagopal K and van der Schee W 2018 *Ann. Rev. Nucl. Part. Sci.* **68** 339
[12] Senger P 2021 Heavy-Ion Collisions at FAIR-NICA Energies *Particles* **4** 214–226
[13] Waqas M and Peng G-X 2021 *Entropy* **23** 488
[14] Derradi de Souza R, Koide T and Kodama T 2016 *Prog. Part. Nucl. Phys.* **86** 35
[15] karimabadi M, Kord A F and Azadegan B 2025 *Eur. Phys. J. A* **61** 22
[16] Pal S and Pratt S 2004 *Phys. Lett. B* **578** 310
[17] Waqas M, Liu F-H, Fakhraddin S and Rahim M A 2019 *Indian J. Phys.* **93** 1329
[18] Babanezhad M, Marjani A and Shirazian S 2020 *Scientific Reports Volume* **16719** 21502
[19] Adam J *et al* 2020 *Phys. Rev. C* **102** 034909
[20] Abgaryan V *et al* 2022 *Eur. Phys. J. A* **58** 140
[21] Teodorescu L and Sherwood D 2008 *Comput.Phys.Commun.* **178** 409
[22] Teodorescu L 2006 *IEEE T. Nucl. Sci.* **53** 2221
[23] Link J M 2005 *Nucl. Instrum. Meth. A* **551** 504
[24] El-Bakry S Y and Radi A 2007 *Int. J. Mod. Phys. C* **18** 351
[25] El-dahshan E, Radi A and El-Bakry M Y 2009 *Int. J. Mod. Phys. C* **20** 1817
[26] Whiteson S and Whiteson D 2009 *Eng. Appl. Artif. Intel.* **22** 1203
[27] Hagan M T and Menhaj M B 1994 *IEEE Trans. Neural Netw.* **6** 861
[28] Thike P, Zhao Z, Shi P and JIN Y 2020 *Bull. Mater. Sci.* **43** 22
[29] Mohamed R A 2022 *Eur. Phys. J. Plus.* **137** 384
[30] Dilek Duranoğlu K and Sinan Altin E 2024 *Heliyon* **10** 2405
[31] Karaboga D and Kaya E 2019 *Artif. Intell. Rev.* **52** 2263–93
[32] Habashy D M and Lebda H I 2022 *Computational Physics* 19
[33] Yassin H, Elyazeed E R A and Tawfik A N 2020 *Phys. Scripta* **95** 7
[34] Cleymans J 2017 *J. Phys. Conf. Ser.* **779** 012079
[35] Bhattacharyya T, Cleymans J, Marques L, Mogliacci S and Paradza M W 2018 *J. Phys. G* **45** 055001
[36] Nedorezov E V, Parvan A S and Aparin A A 2024 *Phys. Part. Nucl.* **55** 984
[37] Zhang P-C, Yang P-P, Duan T-T, Zhu H, Liu F-H and Olimov K K 2025 Comparing effective temperatures in standard and Tsallis distributions from transverse momentum spectra in small collision systems 1 arXiv:2506.00339v2 https://arxiv.org/pdf/2506.00339
[38] Krisut P and Yoo-Kong S 2024 Deriving Tsallis entropy from non-extensive Hamiltonian within a statistical mechanics framework 1 arXiv:2411.16757 https://arxiv.org/pdf/2411.16757
[39] Sollfrank J and Heinz U W 1992 *Phys. Lett. B* **289** 132
[40] Muller B and Rajagopal K 2005 *Eur. Phys. J. C* **43** 15
[41] Gubser S S, Pufu S S and Yarom A 2008 *Phys. Rev. D* **78** 066014
[42] Nonaka C, Muller B, Bass S A and Asakawa M 2005 *Phys. Rev. C* **71** 051901
[43] Berges J, Reygers K, Tanji N and Venugopalan R 2017 *Phys. Rev. C* **95** 054904
[44] Rashid S K A 2024 *KSCE J. Civ. Eng.* **28** 484494
[45] Thinh D D N T 2014 *Adv. Intel. Syst. Comput.* **274** 939947
[46] Deng C, Abdalla A N, Ibrahim T K, Jiang M, Al-Sammarraie A T and Wu J 2020 *Adv. High Energy Phys.* **2020** 6590138

[47] Brehmer J, Louppe G, Pavez J and Cranmer K 2020 *Proc. Nat. Acad. Sci.* **117** 5242
[48] Pang L-G, Zhou K, Su N, Petersen H, Stöcker H and Wang X-N 2018 *Nature Commun.* **9** 210
[49] Pratt S 1984 *Phys. Rev. Lett.* **53** 1219
[50] Bertsch G F 1994 *Phys. Rev. Lett.* **72** 2349 [Erratum: Phys.Rev.Lett. 77, 789 (1996)]
[51] Soff S, Bass S A, Hardtke D H and Panitkin S Y 2002 *Phys. Rev. Lett.* **88** 072301
[52] Cheremnova M, Chernyshov A, Khyzhniak Y, Kodolova O, Kuzmin V, Lokhtin I, Malinina L, Mikhaylov K and Nigmatkulov G 2022 *Symmetry* **14** 1316
[53] Malinina L, Batyuk P, Cheremnova M, Khyzhniak Y, Kodolova O, Mikhaylov K, Nigmatkulov G and Romanenko G 2021 *Phys. Part. Nucl.* **52** 624
[54] Nigmatkulov G, Batyuk P, Khyzhniak Y, Kodolova O, Malinina L and Mikhaylov K 2020 *J. Phys. Conf. Ser.* **1690** 012132
[55] Batyuk P N, Malinina L V, Mikhaylov K R and Nigmatkulov G A 2020 *Phys. Part. Nucl.* **51** 252
[56] Mikhaylov K, Batyuk P, Kodolova O, Malinina L, Nigmatkulov G and Romanenko G 2019 *EPJ Web. Conf.* **222** 02004
[57] Wielanek D 2017 *Proc. SPIE Int. Soc. Opt. Eng.* **10445** 1044546
[58] Batyuk P, Karpenko I, Lednicky R, Malinina L, Mikhaylov K, Rogachevsky O and Wielanek D 2017 *Phys. Rev. C* **96** 024911
[59] Ferenc D, Heinz U W, Tomasik B, Wiedemann U A and Cramer J G 1999 *Phys. Lett. B* **457** 347
[60] Letessier J and Rafelski J 2002 *Hadrons and Quark- Gluon Plasma* (Cambridge University Press)
[61] Aboozar K and Hamid M 2010 *Expert Syst. Appl.* **37** 3070–4 https://dblp.org/rec/journals/eswa/KhajehM10
[62] Himanshu Kumar Jangir and Satavalekar Rupali 2022 *J. Soft Comput. Civ. Eng.* **6** 119–139
[63] Al-Abduljabbar A, Gamal H and Elkatatny S 2020 *Arab J. Geosci.* **13** 784
[64] Adamczyk L *et al* 2017 *Phys. Rev. C* **96** 044904
[65] Hiller G *et al* 2021 *Phys. Rep.* **894** 1
[66] Mehta P, Bukov M, Wang C-H, Day A G R, Richardson C, Fisher C K and Schwab D J 2019 *Phys. Rep.* **810** 1